PAPER

Check for updates

Zinc-induced polycrystalline transformation of high-entropy fluorides and derived regulatory mechanisms for bifunctional oxygen electrocatalysis†

Gang Wang,[a] Hao Chi,[a] Yang Feng,[b] Jie Fan,[a] Nanping Deng,*[a] Weimin Kang [ID] *[a] and Bowen Cheng [ID] *[c]

Designing efficient, stable and low-cost bifunctional oxygen electrocatalysts for metal air batteries is crucial and challenging. The study reports a simple and controllable synthesis strategy of polycrystalline high entropy fluoride modified porous carbon nanofibers ((MnNiCuCoZn)F$_2$-PCNFs) for bifunctional oxygen electrocatalysis. The (MnNiCuCoZn)F$_2$-PCNFs feature continuous and facilitated pathways and a porous structure for electron transportation and mass diffusion, providing an ideal environment for electrocatalytic reactions. The multi-principal element characteristic of high-entropy fluoride also offers a wealth of active sites to enhance the oxygen reduction reaction (ORR) and oxygen evolution reaction (OER). The zinc component leads to the transformation of high-entropy fluoride nanoparticles from single-crystal to polycrystalline, thereby effectively increasing the likelihood of exposing electrocatalytically active sites. Therefore, the prepared (MnNiCuCoZn)F$_2$-PCNFs exhibit superior electrocatalytic performance for the ORR ($E_{1/2}$ = 0.852 V) and OER (η_{10} = 310 mV). The assembled (MnNiCuCoZn)F$_2$-PCNF-based ZABs achieve a high peak power density of 206 mW cm^{-2} and stable operation for more than 400 h. The corresponding DFT calculations further reveal that the zinc component in (MnNiCuCoZn)F$_2$-PCNFs can lead to a continuous distribution of the density of electronic states at the Fermi level, thereby facilitating electron transfer. It can also significantly optimize the energy layout of reaction intermediates, substantially reducing the energy barriers for the ORR and OER (from 1.80 eV to 1.03 eV for the ORR and from 1.35 eV to 0.73 eV for the OER). The study proposes a "polycrystalline transition" that paves a novel pathway for the structural design of high-entropy nanoparticles and holds significant importance for the development of advanced multifunctional electrocatalysts.

1 Introduction

The continued rise in global temperatures brings severe challenges to environmental security.[1,2] Zinc–air batteries (ZABs) have received extensive research attention due to their high theoretical energy density, abundant zinc metal reserves, good rechargeability, low manufacturing cost, high safety and environmental friendliness.[3–5] However, the oxygen evolution reaction (OER) and oxygen reduction reaction (ORR) occurring in

the cathode of ZABs mainly rely on the scarcity and high cost of noble metal electrocatalysts (such as Pt, Ir, Ru, *etc*).[6–8] To this end, various cheap electrocatalysts with excellent activity, high selectivity and good stability have been developed and applied by scientists, such as nanocarbon catalysts,[9] metal/carbon catalysts,[10] transition metal compounds,[11–13] atomically dispersed metal site catalysts,[14,15] MOF-derived material catalysts,[16] high-entropy catalysts[17,18] and so on.

For a long time, in the field of electrocatalysts and ZAB application, the mainstream ideas have been to achieve high catalytic activity of materials through using various modification methods such as heteroatom doping,[19] single atom modification,[20] oxygen vacancy engineering,[21] *etc*. The emerging field of high-entropy materials (HEMs) brings new ideas and attempts to understand what material properties will occur at the limit of extreme disorder.[22] In HEMs, various elements are mixed in roughly equal-atomic proportions, and disorder is no longer a weak perturbation but a dominant effect. Currently, four main

[a]State Key Laboratory of Separation Membranes and Membrane Processes, School of Textile Science and Engineering, Tiangong University, Tianjin, 300387, PR China. E-mail: dengnanping@tiangong.edu.cn; kangweimin@tiangong.edu.cn

[b]State Key Laboratory of Advanced Chemical Power Sources, College of Chemistry, Nankai University, Tianjin 300071, PR China

[c]School of Material Science and Engineering, Tiangong University, Tianjin 300387, PR China. E-mail: bowen15@tiangong.edu.cn

† Electronic supplementary information (ESI) available. See DOI: https://doi.org/10.1039/d4ta02866j

This journal is © The Royal Society of Chemistry 2024

J. Mater. Chem. A, 2024, **12**, 19109–19122 | **19109**

effects of HEMs have been widely accepted, namely the high entropy effect, lattice distortion, sluggish diffusion and the cocktail effect.[23] Specifically, the advantages corresponding to these effects are as follows: (i) the high entropy effect reflects the main contribution of mixing entropy to the formation of a homogeneous phase and improves the thermodynamic stability of the catalyst.[24] (ii) Lattice distortion is due to the size differences between various atoms in HEMs causing the lattice points to deviate from the ideal position.[25] (iii) The sluggish diffusion effect means that lattice distortion leads to an increase in the diffusion activation energy of atoms in the lattice, thereby reducing the effective diffusion rate of atoms and improving the dynamic stability of the catalyst.[26] (iv) The "cocktail" effect refers to a synergistic effect brought about by the interaction between various elements, which can construct a more ideal electronic structure to achieve efficient catalysis.[27] All of these factors can provide HEMs with versatile merits, thus making them widely used in electrocatalytic systems.[28–30] As everyone knows, HEMs can be classified into high-entropy alloys (HEAs), which exist only as metal atoms, and high-entropy compounds (HECs), which exist in the form of compounds. The structure formed by the interaction of multiple elements on the surface of high-entropy materials creates a wide range of potential atomic configurations, which leads to high-entropy alloys demonstrating that enhanced oxygen catalytic performance can be realized.[31] For example, Chen et al.[32] employed a metallurgical approach to develop a $(CrFeCoNi)_{97}O_3$ bulk O-HEA, demonstrating exceptional electrocatalytic performance for the OER. The coordination of some anions to form HECs is an effective method to further improve the oxygen catalytic performance.[33,34] Furthermore, Dai et al.[35] also synthesized a high-entropy fluoride that can exhibit an ultra-low overpotential of 314 mV at 10 mA cm^{-2} for the OER. Due to its highest electronegativity (4.0), fluorine can modulate the electronic properties of the prepared catalyst through a strong charge delocalization effect, thus reducing charge transfer resistance, facilitating fast mass transfer and enhancing oxygen catalysis.[36]

In addition to the above methods being applied to improve oxygen redox performance, various crystal structure design strategies can be employed to enhance the activity of electrocatalysts such as crystal structure porosification,[37] specific crystal facets on single crystals,[38] polycrystalline structures synthesis and so on.[39] For example, Dette et al. designed and prepared polycrystalline hydroxides of Fe/Co/Ni with high roughness which could significantly increase the surface roughness when compared with their single-crystal counterparts, thereby increasing the number of active sites for OER catalysis.[40] Consequently, transferring the polycrystalline transformation strategy to the field of high-entropy materials holds promise for further enhancing their oxygen electrocatalytic activity. In various practical strategies, the atomic rearrangement of crystals with increasing temperature may lead to the transformation from single-crystal to polycrystalline, which is a feasible method among many methods.[41] Inspired by this, introducing zinc with a low melting point into high-entropy materials could result in atomic rearrangement during the calcination process.[42] This may induce the polycrystalline transformation of high-entropy

materials, thus increasing the number of electrocatalytically active sites. However, the zinc-containing high-entropy alloys reported so far have not shown this phenomenon, which may be due to the over-rapid diffusion of zinc in metal particles.[43–45] Therefore, introducing anions to coordinate with metals to enhance the retardation of diffusion in high-entropy materials, and inducing polycrystalline transformation through zinc atomic rearrangement at high temperatures, is a feasible approach. However, no relevant studies have been reported so far.

In this work, a series of middle-high entropy fluoride modified porous carbon nanofibers (($(MnNiCu)F_2$-PCNFs), $(MnNiCuCo)F_2$-PCNFs, $(MnNiCuZn)F_2$-PCNFs, and $(MnNiCoZn)F_2$-PCNFs) were successfully designed and prepared based on electrostatic spinning and calcination for the ORR and OER. The obtained $(MnNiCuCoZn)F_2$-PCNFs with the continuous conductive channels and porous structure, provide an ideal environment for electrocatalytic reactions. The multi-principal element characteristic of high-entropy materials also offers enough active sites, effectively accelerating the electrocatalytic processes of the ORR and OER. Zn transforms high entropy fluoride crystals from single crystal to polycrystalline, which could greatly enhance the contact areas between high entropy fluoride crystals and the liquid electrolyte for more active sites. Therefore, $(MnNiCuCoZn)F_2$-PCNFs exhibit excellent electrocatalytic activity for the ORR ($E_{1/2} = 0.852$ V vs. RHE) and OER ($\eta_{10} = 310$ mV, $\eta_{10} = E_{j=10} - 1.23$ V vs. RHE). The assembled ZABs using the prepared electrocatalysts exhibit a peak power density of 206 mW cm^{-2}, a characteristic capacity of 760 mA h g^{-1}, and a stable charge–discharge cycle capability of more than 400 h. Moreover, the related simulation calculations based on density functional theory have revealed that zinc can also modulate the density of electronic states to facilitate rapid electron transfer, and optimize the energy distribution of the reaction transition state to concurrently lower the energy barriers of both the ORR and OER.

2 Experimental section

2.1 Synthesis of (MnNiCuCoZn)F₂-PCNFs

The detailed preparation process is shown in Fig. 1. Typically, a spinning solution consisting of 4 g polyvinylpyrrolidone (PVP, $Mw = 1\,300\,000$ g mol^{-1}) and 16 g deionized water was mixed in a beaker with a magnetic stirrer for 60 min. Then, 40 g of polytetrafluoroethylene emulsion (PTFE, $Mw = 678.10$ g mol^{-1}, 60 wt%) and a total of 20 mmol of metal salts in an equal molar ratio were added to the above mentioned solution and stirred at room temperature for 3 h. These metal salts included part or all of manganese acetate ($Mn(CH_3COO)_2 \cdot 4H_2O$, MnAc$_2$, 99%), cobalt nitrate ($Co(NO_3)_2 \cdot 6H_2O$, 99%), nickel acetate ($Ni(CH_3COO)_2 \cdot 4H_2O$, NiAc$_2$, 99%), copper nitrate ($Cu(NO_3)_2$, 99%), and zinc acetate ($Zn(CH_3COO)_2 \cdot 4H_2O$, ZnAc$_2$, 99%). Subsequently, the prepared solution was transported to a self-built electro-blowing spinning device (EBS) for producing the precursor nanofibers at a voltage of 20 kV, a distance between the nozzle and the collector of 800 mm, and an air pressure of 0.1 MPa. Subsequently, the precursor nanofibers were transferred to a muffle furnace and heated to 250 °C at a rate of 2 °C min^{-1} in

19110 | J. Mater. Chem. A, 2024, 12, 19109–19122

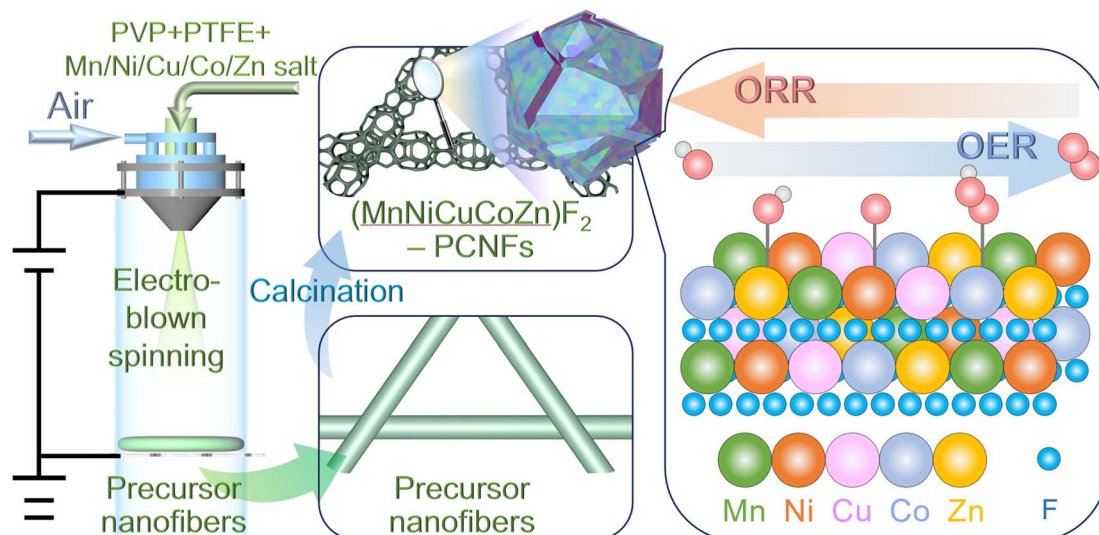This journal is © The Royal Society of Chemistry 2024

Fig. 1 Schematic diagram of the preparation of high entropy fluoride modified porous carbon nanofibers.

an air atmosphere and maintained for 1 h. The pretreated nanofibers were carbonized in a nitrogen atmosphere in a tube furnace by heating to 800 °C at a rate of 2 °C min^{-1} and kept for 1 h. The decomposition of PTFE at high temperatures produces a fluorine-containing atmosphere, which induces the formation of a porous structure.[35,46] Moreover, due to the presence of a fluorine-containing atmosphere, metal salts will have a big opportunity to transform into metal fluorides.[47] The prepared porous carbon nanofibers (PCNFs) loaded with multicomponent metal fluorides were named $(MnNiCu)F_2$-PCNFs, $(MnNiCuCo)F_2$-PCNFs, $(MnNiCuZn)F_2$-PCNFs, and $(MnNiCuCoZn)F_2$-PCNFs according to the elements contained, respectively.

2.2 Electrochemical measurements

The electrochemical measurements were performed using an electrochemical cell equipped with a spinner supplied by PINE Co. The corresponding electrochemical properties were measured using a CHI760e electrochemical workstation of Shanghai Chenhua Company. The working electrodes used include a rotating disk electrode (RDE) with a 5 mm GC disk, a rotating ring disk electrode (RRDE) with a 5.61 mm GC disk and a 7.09 mm platinum ring, and 1 mm thick nickel foam. The applied Hg/HgO electrode was used as the reference electrode, and a carbon rod was used as the counter electrode. All potentials are reported relative to the reference hydrogen electrode (RHE). The used catalyst ink was prepared by mixing 4 mg catalyst, 40 μL Nafion solution and 960 μL ethanol, with a catalyst loading of 0.2 mg cm^{-2} for RDE and RRDE tests. For the assembled zinc–air batteries, the anode consists of high-grade zinc flakes, while the cathode consists of hydrophobic carbon paper coated with catalyst ink (0.5 mg cm^{-2}). The liquid electrolyte used was a mixture of 6 M KOH and 0.2 M ZnAc$_2$. The charge–discharge cycle stability of the assembled battery was evaluated through a series of 10 min charge and 10 min discharge cycles.

2.3 Computational methods

All density functional theory (DFT) calculation results are obtained by running the Vienna *Ab Initio* Simulation Package (VASP). The exchange correlation potential is described using the generalized gradient approximation (GGA) and the spin-polarized Perdew–Burke–Ernzerhof (PBE) functional. The electron/ion interaction relationship is described by the additive plane wave method, and the cutoff plane wave energy was set to 350 eV. Structural relaxation followed the convergence criteria of an energy difference of 10^{-5} eV per atom and a stress difference of 0.02 eV Å^{-1}. To eliminate interactions between adjacent surfaces, a vacuum layer with a thickness of more than 15 Å was introduced. The system energy, electronic density of states (DOS) and charge distribution were calculated based on a single point energy difference of 10^{-7} and a gamma grid K-point configuration of $3 \times 3 \times 2$. In order to achieve more accurate transition metal energy estimation, a simplified (rotation invariant) DFT + U method proposed by Dudalev *et al.*[48,49] was adopted. According to relevant literature, the "U–J" values of Mn, Co, Ni and Cu were set to 4.5, 5.9, 6 and 4.5 respectively.[50–52]

3 Results and discussion

In electrocatalytic processes including the ORR and OER, effective electrocatalysts need to have continuous electron conductivity, abundant electrocatalytically active sites, large specific surface area, and excellent intrinsic electrocatalytic activity to ensure that the electrochemical process proceeds efficiently.[53] The high-resolution transmission electron micrographs of $(MnNiCu)F_2$-PCNFs, $(MnNiCuCo)F_2$-PCNFs, $(MnNiCuZn)F_2$-PCNFs, and $(MnNiCuCoZn)F_2$-PCNFs are shown in Fig. 2. These figures all clearly show that a continuous conductive carbon skeleton can be obtained for these samples. The medium/high entropy fluoride nanoparticles are evenly distributed on the continuous conductive carbon skeleton.
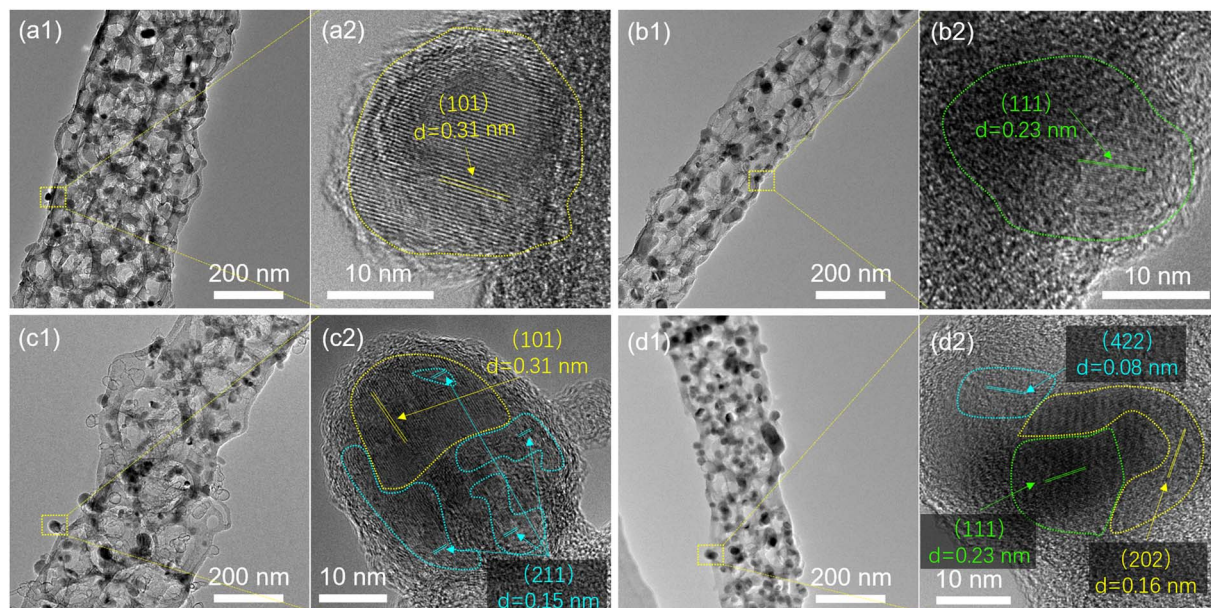
This journal is © The Royal Society of Chemistry 2024

J. Mater. Chem. A, 2024, **12**, 19109–19122 | 19111

Fig. 2 The high-resolution transmission electron micrographs (HR-TEM) of (a1 and a2) $(MnNiCu)F_2$-PCNFs, (b1 and b2) $(MnNiCuCo)F_2$-PCNFs, (c1 and c2) $(MnNiCuZn)F_2$-PCNFs, and (d1 and d2) $(MnNiCuCoZn)F_2$-PCNFs.

These test results show that they all have continuous electron transport pathways for efficient electrocatalytic reactions.

The high-resolution transmission electron micrograph (HR-TEM) of $(MnNiCu)F_2$-PCNFs (Fig. 2a2) can be identified using clear crystal plane diffraction fringes with a spacing of 0.31 nm, so it is speculated that they are the (101) crystal plane of the obtained M/HEFs. The prepared $(MnNiCuCo)F_2$-PCNFs were identified with an interplanar spacing of 0.23 nm, which was speculated to be the (111) crystal plane of the obtained M/HEFs. And in the obtained $(MnNiCuZn)F_2$-PCNFs, two different groups of crystal plane spacings can be identified, which are speculated to be the (101) crystal plane and (211) crystal plane, both of which are belonging to M/HEFs. Among them, the exposed part of the (101) crystal plane has a relatively regular shape. But the divided (211) crystal planes are dispersed throughout the M/HEF, and part of it is even surrounded by the formed (101) crystal plane. The fluoride in the formed $(MnNiCuCoZn)F_2$-PCNFs also exhibits a similar polycrystalline structure in which multiple crystal planes co-exist and stack on each other. However, the crystallographic faces in the prepared (MnNiCuZn)F_2P-CNF can be completely surrounded by other crystallographic faces (higher degree of disorder), and the crystallographic faces in the $(MnNiCuCoZn)F_2$-PCNF are more ordered and aggregated when compared with other M/HEF. In addition, the corresponding selected area electron diffraction (SAED) was performed to further prove whether the crystals were polycrystalline (Fig. S1†). The electron diffraction patterns without rotational symmetry indicate that the single-crystal grain structure of $(MnNiCu)F_2$-PCNFs and $(MnNiCuCo)F_2$-PCNFs can be formed (Fig. S1a and b†).[38] The clearly rotationally symmetric electron diffraction patterns demonstrate that the polycrystalline state of $(MnNiCuZn)F_2$-PCNFs and $(MnNiCuCoZn)F_2$-PCNFs can be realized (Fig. S1a and b†).[54–56] For

exploring the reasons for the formation of the polycrystalline structure, the melting and boiling points of various related substances have been compiled according to the *Lange's Handbook of Chemistry*[42] as shown in Table S1†. The melting and boiling points of each metal fluoride are lower than the corresponding carbonization temperature. The carbonization temperature is higher than the melting point of zinc metal but lower than the melting point of other metals except zinc. The carbonization temperature even approaches the boiling point of zinc metal. Since a large amount of reducing gases such as carbon monoxide will be produced during the carbonization process, they may compete with the fluorine in the fluoride, which may cause the fluoride to be reduced to a metallic state, and then melt or even vaporize, causing internal stress changes, thereby greatly inducing crystal rupture. The formation process may be the reason why the fluoride in the prepared $(MnNiCuZn)F_2$-PCNFs, and the $(MnNiCuCoZn)F_2$-PCNFs can be identified as polycrystals with multiple coexisting crystal faces and stacked on each other. But the fluoride particles in the $(MnNiCu)F_2$-PCNFs and the $(MnNiCuCo)F_2$-PCNFs both present independent crystals with a single crystal plane. The increased exposed surface of particles due to transformation may significantly increase the accessibility of electrocatalytically active sites.[57]

It is therefore necessary to analyze the elemental composition of the sample to further confirm the existence of this effect. The elemental analysis was conducted through an energy-dispersive X-ray spectroscopy (EDS) analysis using an electron microscope (Fig. S2–S5†). From these figures, it is evident that the distribution of the carbon element and the carbon skeleton is highly consistent, confirming the presence of a continuous conductive pathway in the material. The MnNiCu element in the prepared $(MnNiCu)F_2$-PCNFs, the MnNiCuCo element in $(MnNiCuCo)F_2$-PCNFs, the MnNiCuZn element in (MnNiCuZn)

19112 | *J. Mater. Chem. A*, 2024, **12**, 19109–19122

This journal is © The Royal Society of Chemistry 2024

F_2-PCNFs and the MnNiCuCoZn element in (MnNiCuCoZn)F_2-PCNFs all overlap with each other. The fluorine element in each sample is distributed on the skeleton and aggregated at the particles. These pieces of evidence together strongly prove the successful synthesis of multi-metallic fluorides. When comparing the content of each element (Table S2†), carbon still accounts for the absolute majority (>90%), which is rather beneficial to the smooth transmission of electrons. The fluorine element is more than twice that of each metal element, which greatly proves that in addition to metal fluorides, some fluorine is combined with carbon to form fluorine-doped carbon materials. In order to facilitate the comparison of the content of metal elements, the content of each metal element is obtained and depicted in a pie chart (Fig. 3a). It can be seen that the MnNiCu element in (MnNiCu)F_2-PCNFs and the MnNiCuCo element in (MnNiCuCo)F_2-PCNFs both show comparable proportions. The MnNiCuZn element in (MnNiCuZn)F_2-PCNFs and the MnNiCuCoZn element in (MnNiCuCoZn)F_2-PCNFs both show a slightly lower proportion of Zn than MnNiCuCo, and MnNiCuCo are comparable proportions. These test results also further confirm that zinc will be partially lost during the preparation process. In addition, based on previous research reports, the configurational entropy of the obtained (MnNiCu)F_2-PCNFs, (MnNiCuCo)F_2-PCNFs, (MnNiCuZn)F_2-PCNFs, and (MnNiCuCoZn)F_2-PCNFs can be calculated using Formula S3† based on the data from Fig. 3a, which are 1.09R, 1.39R, 1.36R, and 1.60R, respectively.[58] Among them, the configurational entropy of (MnNiCuCoZn)F_2-PCNFs is larger than 1.5R, which can be identified as high-entropy fluorides among these samples.[23,59]

The XRD patterns of the sample is shown in Fig. 3b, and the (MnNiCuCoZn)F_2 model can be constructed according to the metal element ratio of the obtained (MnNiCuCoZn)F_2-PCNFs. The simulated (MnNiCuCoZn)F_2 has an XRD pattern similar to that of the actual (MnNiCuCoZn)F_2-PCNFs, which significantly illustrates successful synthesis of (MnNiCuCoZn)F_2-PCNFs. The prepared (MnNiCuCoZn)F_2-PCNFs exhibit similar independent peaks when compared to the standard card of monometallic fluorides. Compared to the superimposed XRD spectra of individually prepared single-metal fluoride composite PCNFs, the XRD spectra measured from (MnNiCuCoZn)F_2-PCNFs are significantly more consistent with the simulated XRD spectra (Fig. S6†). These results show that it is a new type of fluoride crystal different from single metal fluoride, rather than a simple physical mixture of individual single metal fluorides. The obtained MEF-PCNFs with three or four metal element types have different lattice distortion effects from the obtained (MnNiCuCoZn)F_2-PCNFs due to some differences in the atomic radii of the metal elements. Therefore, they will exhibit inconsistent crystal constants and slightly different XRD patterns.[25]

The pore structure of the material was also tested and characterized through the nitrogen adsorption and desorption curves (Fig. 3c). The corresponding pore size distribution is also given in Fig. 3d. The specific surface area of (MnNiCu)F_2-PCNFs, (MnNiCuCo)F_2-PCNFs, (MnNiCuZn)F_2-PCNFs, and (MnNiCuCoZn)F_2-PCNFs is 166.4 m^2 g^{-1}, 153.0 m^2 g^{-1}, 127.5 m^2 g^{-1} and 101.0 m^2 g^{-1}, respectively. That is, when the metal component is more, it is more likely to block a wider range of micropores.[60] When compared with micropores and macropores, mesopores have more advantages in mass transfer, gas transport and liquid electrolyte penetration.[61,62] The mesopore volumes for (MnNiCu)F_2-PCNFs, (MnNiCuCo)F_2-PCNFs, (MnNiCuZn)F_2-PCNFs, and (MnNiCuCoZn)F_2-PCNFs are 0.284 cc g^{-1}, 0.252 cc g^{-1}, 0.285 cc g^{-1}, and 0.275 cc g^{-1}, respectively. The mesoporous fraction of (MnNiCuCoZn)F_2-PCNFs, with the highest being 0.285 cc g^{-1}, differed by less than 5%. Referring to related work already reported, it can be inferred that the mesoporous structure of (MnNiCuCoZn)F_2-PCNFs is approximately equivalent to that of the other samples to a certain extent.[63–66]
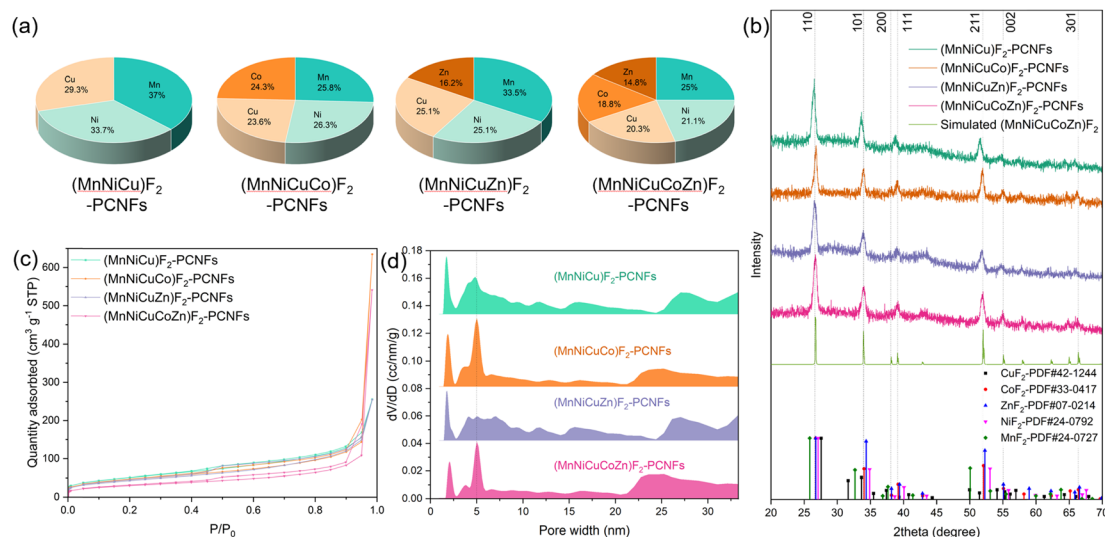

Fig. 3 (a) The content of each metal element in the sample (atomic%). (b) The X-ray diffraction (XRD) pattern. (c) The nitrogen adsorption–desorption curves and (d) pore size distribution diagrams.

This journal is © The Royal Society of Chemistry 2024

J. Mater. Chem. A, 2024, **12**, 19109–19122 | **19113**

The binding energies (B.E.) can be tested through X-ray photoelectron spectroscopy (XPS) for composition characterization and the electronic state (Fig. 4 and S7†). The deconvolution results of Mn-2p show that the Mn-$2p^{3/2}$ of each sample appears at around 642.7 eV, among which the Mn-$2p^{3/2}$ of $(MnNiCuCo)F_2$-PCNFs shifts positively by 0.1 eV when compared to that of other samples. The deconvolution results of Ni-2p show that the B.E. of Ni-$2p^{2/3}$ in the $(MnNiCu)F_2$-PCNF increases from 857.2 eV to 857.5 eV and 857.4 eV in the case of Co and Zn doping, respectively. When Co and Zn are doped at the same time, the B.E. of Ni-$2p^{3/2}$ further shifts positively to 857.7 eV, which shows that the doping of Co and Zn can further reduce the electron density of nickel in multi-component fluorides. Some studies suggest that this reduction in electron density is beneficial to the progress of nucleophilic reactions (such as the OER under alkaline conditions).[67,68] The B.E. of Cu-$2p^{3/2}$ moves negatively from 934.1 eV of the prepared $(MnNiCu)F_2$-PCNFs to 933.5 eV of the obtained $(MnNiCuCo)F_2$-PCNFs, 933.8 eV of the prepared $(MnNiCuZn)F_2$-PCNFs and 933.8 eV of the obtained $(MnNiCuCoZn)F_2$-PCNFs, respectively.[69] These test results also reflect that the electron density of copper atoms can be increased due to the doping of Co and Zn to greatly promote electrophilic reactions (such as the ORR under alkaline conditions).[67] A relatively obvious Co-$2p^{3/2}$ peak can be identified in both the prepared $(MnNiCuCo)F_2$-PCNFs and $(MnNiCuCoZn)F_2$-PCNFs near 782.5 eV.[70] For the $(MnNiCuZn)F_2$-PCNFs and $(MnNiCuCoZn)F_2$-PCNFs, the Zn-$2p^{3/2}$ peak is identified near 1022.4 eV, which strongly reflects that successful doping of Zn can be realized.[71] The F-1s energy spectra of all samples can be decomposed into C–F bonds at 687.0 eV and ionic metal-fluorine bonds (M–F) at 684.7 eV.[72]

The ORR activities of the prepared catalysts are measured using a typical three-electrode system in 0.1 M KOH, where all potentials are calibrated to the potential relative to RHE. The polarization current curves and the corresponding Tafel slopes are shown in Fig. 5a and b. As for $(MnNiCuCoZn)F_2$-PCNFs, the onset potential (E_0) is 0.899 V, the half-wave potential ($E_{1/2}$) is 0.852 V, and the limit current density (J_L) is 5.52 mA cm^{-2}. The ORR activities of $(MnNiCuCoZn)F_2$-PCNFs are slightly lower than that of the commercial Pt/C catalyst ($E_0 = 0.926$ V, $E_{1/2} = 0.856$ V, and $J_L = 5.50$ mA cm^{-2}), but these performances are superior to those of the $(MnNiCuZn)F_2$-PCNFs ($E_0 = 0.883$ V, $E_{1/2} = 0.740$ V, and $J_L = 4.84$ mA cm^{-2}), the $(MnNiCuCo)F_2$-PCNFs ($E_0 = 0.875$ V, $E_{1/2} = 0.782$ V, and $J_L = 4.35$ mA cm^{-2}), and the $(MnNiCu)F_2$-PCNFs ($E_0 = 0.831$ V, $E_{1/2} = 0.758$ V, and $J_L = 3.49$ mA cm^{-2}). When compared to the $(MnNiCu)F_2$-PCNFs, the obtained $(MnNiCuZn)F_2$-PCNFs exhibit a higher E_0 and a significant improvement in J_L. Therefore, it is speculated that the addition of zinc components significantly enhances the variety and number of active sites in the prepared $(MnNiCuZn)F_2$-PCNFs. Moreover, the $(MnNiCuCo)F_2$-PCNFs show higher E_0, $E_{1/2}$, and J_L when compared to the $(MnNiCu)F_2$-PCNFs, indicating that the incorporation of cobalt components significantly enhances the intrinsic activity and quantity of ORR active sites in the $(MnNiCuCo)F_2$-PCNFs. Unlike the dispersed pore size distribution of $(MnNiCuZn)F_2$-PCNFs, the $(MnNiCuCo)F_2$-PCNFs constructed a more concentrated mesoporous structure with a pore size of about 5 nm, which may be related to the enhancement of ORR intrinsic activity. The obtained $(MnNiCuCoZn)F_2$-PCNFs exhibit a combination of the features of $(MnNiCuCo)F_2$-PCNFs and $(MnNiCuZn)F_2$-PCNFs, forming a concentrated mesoporous structure with a 5 nm pore size and transformed fluoride crystals. The formed unique structure endows the prepared $(MnNiCuCoZn)F_2$-PCNFs with enhanced ORR intrinsic activity and more ORR active sites. The Tafel slope of $(MnNiCuCoZn)F_2$-PCNFs is 83.4 mV dec^{-1}, which is
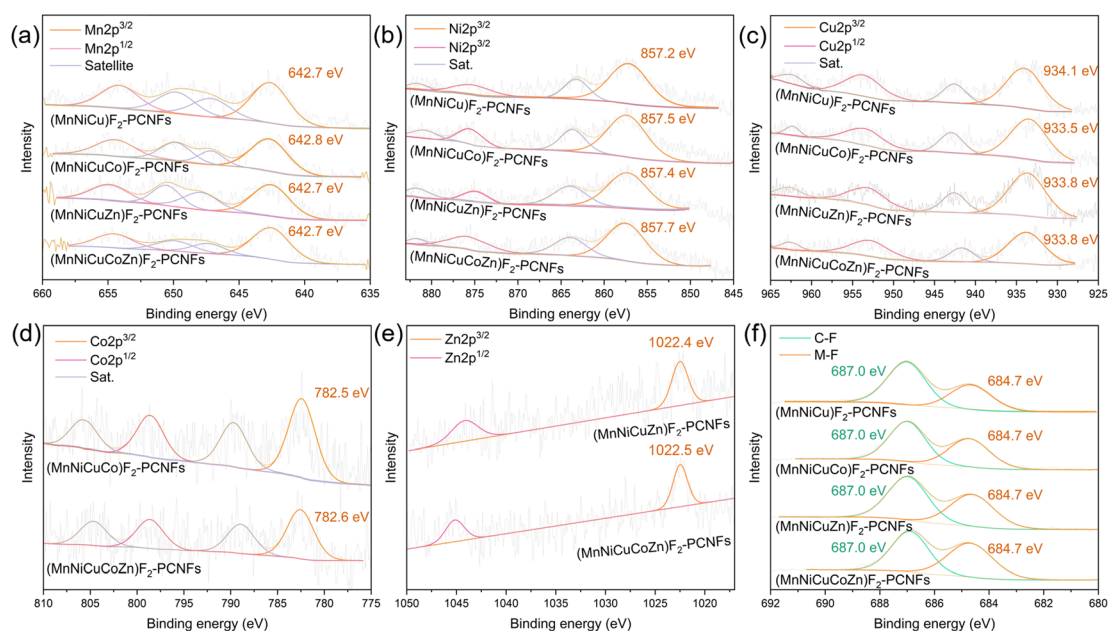

Fig. 4 High-resolution X-ray photoelectron spectra. (a) Mn-2p, (b) Ni-2p, (c) Cu-2p, (d) Co-2p, (e) Zn-2p, and (f) F-1s.

19114 | J. Mater. Chem. A, 2024, 12, 19109–19122

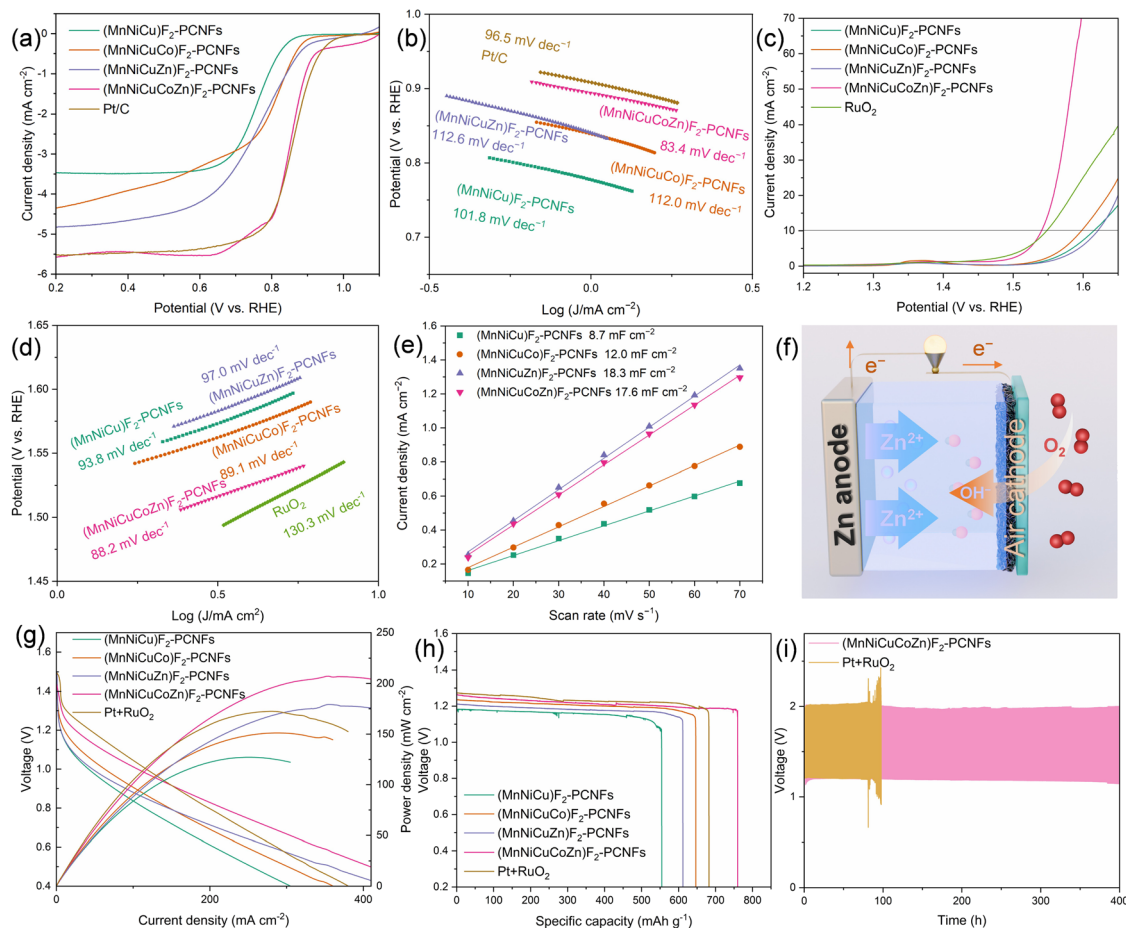This journal is © The Royal Society of Chemistry 2024

Fig. 5 (a) Polarization curves and (b) corresponding Tafel slopes for the ORR. (c) OER performance and (d) corresponding Tafel slopes. (e) C_{dl} fitting curves. (f) Schematic of a ZAB, (g) discharge polarization curves and corresponding power density curves, (h) continuous discharge curves, and (i) charge−discharge cycles.

lower than that of the $(MnNiCuCo)F_2$-PCNFs (96.5 mV dec^{-1}), the $(MnNiCuZn)F_2$-PCNFs (112.6 mV dec^{-1}), the $(MnNiCu)F_2$-PCNFs (101.8 mV dec^{-1}), and even the commercial Pt/C (96.5 mV dec^{-1}), suggesting that the $(MnNiCuCoZn)F_2$-PCNFs exhibit rapid ORR kinetics.[73] Furthermore, as shown in Fig. S8,† the n value of $(MnNiCuCoZn)F_2$-PCNFs is approximately 4, which is higher than that of the obtained $(MnNiCuCo)F_2$-PCNFs, $(MnNiCuZn)F_2$-PCNFs, and $(MnNiCu)F_2$-PCNFs, indicating that a high four-electron selectivity towards the ORR for $(MnNiCuCoZn)F_2$-PCNFs can be obtained.[74]

For the OER (Fig. 5c and d), the $(MnNiCuCoZn)F_2$-PCNFs exhibit an overpotential ($\eta_{10} = E_{j=10} - 1.23$ V) of 310 mV, which is lower than that of RuO_2 (318 mV), the $(MnNiCuCo)F_2$-PCNFs (368 mV), the $(MnNiCuZn)F_2$-PCNFs (391 mV), and the $(MnNiCu)F_2$-PCNFs (385 mV). When compared to the $(MnNiCu)F_2$-PCNFs, the $(MnNiCuZn)F_2$-PCNFs show an increased η_{10} but also a higher current density at 1.65 V, suggesting that the introduction of Zn can increase the number of OER active sites in the $(MnNiCuZn)F_2$-PCNFs, but with a slightly weaker intrinsic activity. The results can be mainly attributed to some differences in pore size distribution and particle integrity between the $(MnNiCuZn)F_2$-PCNFs and the $(MnNiCu)F_2$-PCNFs. The introduction of Co in the $(MnNiCuCo)F_2$-PCNFs results in

a lower η_{10} and a higher current density at 1.65 V vs. RHE compared to the $(MnNiCu)F_2$-PCNFs, reflecting the enhanced intrinsic OER catalytic activity due to Co incorporation. The synergistic effect of Co and Zn components in the $(MnNiCuCoZn)F_2$-PCNFs leads to a significantly lower η_{10} and enhanced current density at 1.65 V vs. RHE compared to those of the $(MnNiCuCo)F_2$-PCNFs, the $(MnNiCuZn)F_2$-PCNFs, and the $(MnNiCu)F_2$-PCNFs. Comparison of the Tafel slopes reveals the following order: $(MnNiCuCoZn)F_2$-PCNFs (88.2 mV dec^{-1}) < $(MnNiCuCo)F_2$-PCNFs (89.1 mV dec^{-1}) < $(MnNiCu)F_2$-PCNFs (93.8 mV dec^{-1}) < $(MnNiCuZn)F_2$-PCNFs (97.0 mV dec^{-1}), which is in complete agreement with the above analysis and further confirms the synergistic effect of Co and Zn components. The Tafel slope of $(MnNiCuCoZn)F_2$-PCNFs, being lower than that of RuO_2 (130.3 mV dec^{-1}), also demonstrates its superior OER kinetics.[75,76] After 2000 cycles of accelerated durability testing (ADT), the η_{10} of $(MnNiCuCoZn)F_2$-PCNFs increases by 18 mV, whereas that of RuO_2 increases by 20 mV (Fig. S9†), indicating that a stable and excellent OER performance of $(MnNiCuCoZn)F_2$-PCNFs can be realized.

The electrochemical surface area (ECSA) is defined as the actual effective area on the electrode material that can participate in electrochemical reactions.[77] The parameter is crucial for

This journal is © The Royal Society of Chemistry 2024

J. Mater. Chem. A, 2024, **12**, 19109–19122 | **19115**

assessing the electrocatalytic efficiency of electrode materials, as the rate of electrochemical reactions is typically directly related to the material's effective surface area.[78,79] The capacitance value is obtained by calculating at different scan rates within the non-faradaic current range. The CV curves at different scan rates within the non-faradaic current range for these prepared $(MnNiCu)F_2$-PCNFs, $(MnNiCuCo)F_2$-PCNFs, $(MnNiCuZn)F_2$-PCNFs, and $(MnNiCuCoZn)F_2$-PCNFs are shown in Fig. S10.† Fitting the central intercept of their CV curves yields their double-layer capacitance (C_{dl}) (Fig. 5e). The C_{dl} of $(MnNiCuCoZn)F_2$-PCNFs is 17.6 mF cm^{-2}, which is essentially equivalent to the 18.3 mF cm^{-2} of $(MnNiCuZn)F_2$-PCNFs, and higher than the 12.0 mF cm^{-2} of $(MnNiCuCo)F_2$-PCNFs and the 8.7 mF cm^{-2} of $(MnNiCu)F_2$-PCNFs, indicating that zinc contributes more to the C_{dl} than cobalt. The reason is speculated to be related to zinc inducing a polycrystalline transition in the fluoride, leading to more accessible electrochemical reaction sites.[39] Based on the measurement results of C_{dl}, the ECSA was calculated and used to normalize the OER catalytic performance.[80,81] The normalized polarization curves from the ECSA also revealed the superiority of the $(MnNiCuCoZn)F_2$-PCNFs among these samples (Fig. S11†).[80] Electrochemical Impedance Spectroscopy (EIS) is employed to reveal the charge transfer capabilities of the prepared catalysts and to discuss their impact on the electrocatalytic activity. The measured Nyquist plots, as shown in Fig. S12,† generally indicate a positive correlation between the semicircle diameter and the charge transfer impedance.[82] Consequently, the order of magnitude for charge transfer impedance is as follows: $(MnNiCuCoZn)F_2$-PCNFs < $(MnNiCuCo)F_2$-PCNFs < $(MnNiCu)F_2$-PCNFs < $(MnNiCuZn)F_2$-PCNFs. This order inversely correlates with their OER activity trends, suggesting that smaller charge transfer impedance is conducive to faster OER kinetics.[83]

Structural stability is crucial for the catalytic performance of catalysts. The long-term stability of $(MnNiCuCoZn)F_2$-PCNFs for the OER was tested as shown in Fig. S13.† The prepared $(MnNiCuCoZn)F_2$-PCNFs exhibited a 94% current density, which was significantly superior to the 76% of RuO_2. The XRD test result of $(MnNiCuCoZn)F_2$-PCNFs after a 20 000-second OER process also confirmed that the stable existence of high-entropy fluorides can be obtained (Fig. S14†). Moreover, the microstructure of $(MnNiCuCoZn)F_2$-PCNFs after the OER process was carefully observed using the HR-TEM testing equipment (Fig. S15†). The prepared $(MnNiCuCoZn)F_2$-PCNFs still displayed their original nanofiber conductive pathways even after the OER (Fig. S15a†). Additionally, the polycrystalline structure of the high-entropy fluorides was demonstrated by the rotation of electron diffraction spots in the SAED pattern (Fig. S15b2†).[54–56] Furthermore, a linear scanning of EDS on the $(MnNiCuCoZn)F_2$-PCNFs after the OER also revealed that a distinct high-intensity signal of the oxygen element at the crystal interfaces of the polycrystalline $(MnNiCuCoZn)F_2$ particles can be realized (Fig. S15d†). All of these proved that the crystal interfaces of the polycrystalline particles were more likely to participate in the OER, thereby generating oxygen-containing intermediates.[84]

The practical application of the prepared catalysts is evaluated by assembling them into ZABs (Fig. 5f). Initially, their discharge polarization curves are obtained, and the power density curves are obtained (Fig. 5g). The $(MnNiCuCoZn)F_2$-PCNF-based-ZAB exhibits a peak power density of 206 mW cm^{-2}, which is higher than that of the $(MnNiCuZn)F_2$-PCNF-based-ZAB (178 mW cm^{-2}), the $(MnNiCuCo)F_2$-PCNF-based-ZAB (151 mW cm^{-2}), and the $(MnNiCu)F_2$-PCNF-based-ZAB (127 mW cm^{-2}), and even surpasses that of the Pt/C + RuO_2-based-ZAB (172 mW cm^{-2}). These results demonstrate the effective power release capability of the $(MnNiCuCoZn)F_2$-PCNFs as a cathode catalyst for ZABs. As depicted in Fig. 5h, the $(MnNiCuCoZn)F_2$-PCNF-based-ZAB exhibits a specific capacity of 760 mA h g^{-1}, exceeding that of the $(MnNiCuZn)F_2$-PCNF-based-ZAB (611 mA h g^{-1}), the $(MnNiCuCo)F_2$-PCNF-based-ZAB (647 mA h g^{-1}), and the $(MnNiCu)F_2$-PCNF-based-ZAB (555 mA h g^{-1}), and even outperforming the Pt/C + RuO_2-based-ZAB (682 mA h g^{-1}). All of these results reflect the highest specific capacity output capability of the $(MnNiCuCoZn)F_2$-PCNFs as a cathode catalyst for ZABs among the prepared samples. Moreover, the $(MnNiCuCoZn)F_2$-PCNF-based-ZAB is able to operate for over 400 h (Fig. 5i), significantly surpassing the Pt/C + RuO_2-based-ZAB. In comparison to some related studies reported in Table S3,† the $(MnNiCuCoZn)F_2$-PCNFs prepared in this study exhibited a superior potential gap ($\Delta E = E_{j=10} - E_{1/2} = 0.688$ V) and a higher peak power density of 206 mW cm^{-2}. This demonstrates the broad application prospects of the $(MnNiCuCoZn)F_2$-PCNFs as bifunctional oxygen electrocatalysts.

For understanding the impact of electronegativity differences among various metals in HEAs on driving the adsorption and conversion of intermediates in alkaline ORR and OER, we proposed the potential adsorption state models and schematic diagrams of reaction processes based on classical electrochemical oxygen catalysis theory.[53,85] As shown in Fig. 6a, under alkaline conditions, the OER process involves the interaction of H_2O with the catalyst, successively generating *OH, *O, and *OOH transition states, eventually converting to O_2.[86] The ORR process is the reverse reaction of the OER process, where the interaction of O_2 with the catalyst successively generates *OOH, *O, and *OH transition states, eventually converting to H_2O. Based on the results of the preliminary component analysis, a structural model with a constant metal atom ratio $(MnNiCuCoZn)F_2$ was constructed, as shown in Fig. 6b.

Based on the results of preliminary compositional analysis, we constructed a model with a constant metal atomic ratio, $(MnNiCuCoZn)F_2$, exhibiting a tetragonal symmetry structure. The $(MnNiCuCoZn)F_2$ model with tetragonal symmetry is shown in Fig. 6b. It is generally believed that oxygenated transition states will only adsorb on metal atomic sites, so we conducted an analysis of the partial density of states (PDOS) for the metal elements (Fig. 6c and d). Compared to the isolated density of electronic states near E_F in $(MnNiCuCo)F_2$, $(MnNiCuCoZn)F_2$ exhibits a continuous distribution of electronic states near E_F, which further illustrates that the low charge transfer resistance of $(MnNiCuCoZn)F_2$ can be obtained.[87,88]

19116 | *J. Mater. Chem. A*, 2024, **12**, 19109–19122
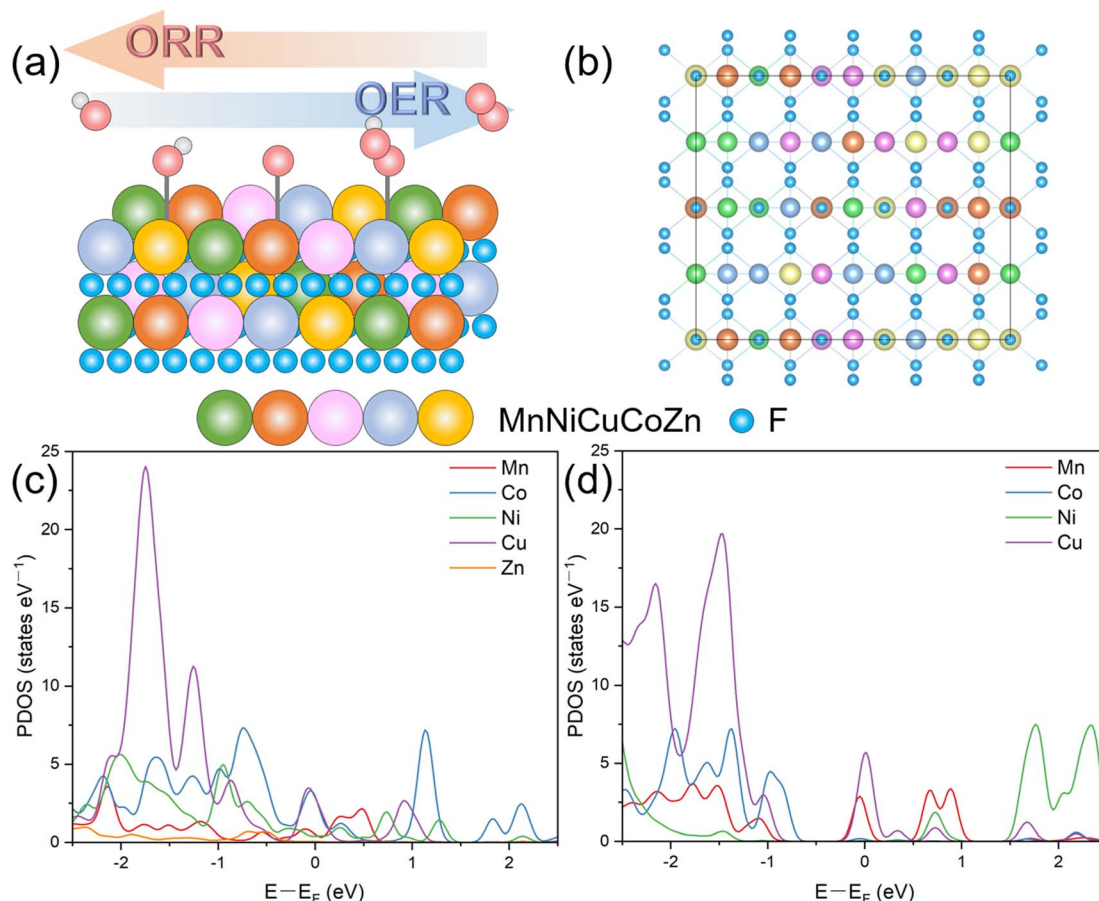
This journal is © The Royal Society of Chemistry 2024

Fig. 6 The adsorption state model and reaction process schematic diagram of (a) the OER/ORR process and (b) the structure model of $(MnNiCuCoZn)F_2$. Partial Density of States (PDOS) diagrams for (c) $(MnNiCuCoZn)F_2$ and (d) $(MnNiCuCo)F_2$.

The ORR process involves the dissociation of the O–O bond in O_2 and adsorption on the metal site surface, followed by multiple protonation steps to form oxygenated intermediates (*i.e.*, *OOH, *O, and *OH) and H_2O.[89] The adsorption energies for each possible step on each metal site of $(MnNiCuCoZn)F_2$ are shown in Fig. 7a, with each energy value corrected through $U = -1.23$ V to eliminate the effect of the standard potential.[53] The calculated results indicate that the energy barrier of the rate-determining step (RDS) on the Co site exhibits a ΔG value of 0.60 eV, which is lower than those on Zn ($\Delta G = 3.33$ eV), Cu ($\Delta G = 0.80$ eV), Ni ($\Delta G = 3.92$ eV), and Mn ($\Delta G = 1.80$ eV) sites. Therefore, Co sites in $(MnNiCuCoZn)F_2$ can offer better ORR catalytic activity when compared to other metal sites. The RDS energy barrier on Zn sites is significantly higher than those on Cu and Co, indicating that the ORR activity contributed by Zn sites is very limited. Additionally, a model with a constant metal atomic ratio for $(MnNiCuCo)F_2$ is also constructed and the derived oxygenated intermediates for each metal site are simulated to obtain the energy distribution (Fig. 7b). The comparison between $(MnNiCuCo)F_2$ and $(MnNiCuCoZn)F_2$ helps elucidate the role of Zn components in mid-entropy fluorides. Herein, Co sites exhibit the lowest energy barrier for the RDS in the ORR ($\Delta G = 1.03$ eV) among these samples, which is lower than those for Cu ($\Delta G = 2.87$ eV), Ni ($\Delta G = 1.65$ eV), and

Mn ($\Delta G = 2.34$ eV). The addition of Zn components leads to a reduction in the energy of derived oxygenated intermediates on Co sites of $(MnNiCuCoZn)F_2$, with the RDS involving the protonation move from *OOH to *OH. The results further lead to a significantly lower ΔG value for Co sites in $(MnNiCuCoZn)F_2$ when compared to $(MnNiCuCo)F_2$, strongly proving that the higher ORR activity of $(MnNiCuCoZn)F_2$ also stems from Zn's improvement of the electronic structure. Hence, Co components dominate the ORR catalytic process in the $(MnNiCuCoZn)F_2$-PCNFs. Besides affecting the pore structure characteristics of PCNFs and causing transformation of the $(MnNiCuCoZn)F_2$ nanoparticles to expose more active sites, zinc's role in electronic regulation on other metal sites can further enhance ORR catalytic activity.

The OER process involves the adsorption of H_2O on the surface of metal sites, followed by multiple deprotonation steps and O–O coupling to form oxygenated intermediates (*i.e.*, *OH, *O, and *OOH) and O_2.[89] The OER processes of $(MnNiCuCoZn)F_2$ and $(MnNiCuCo)F_2$ are shown in Fig. 7c and d. The deprotonation of *OH to form the *O species, as well as the combination of *O with H_2O and subsequent deprotonation to form *OOH species, may be challenging and act as the possible RDS (Rate-Determining Steps) for metal sites in both $(MnNiCuCo)F_2$ and $(MnNiCuCoZn)F_2$. The energy barrier of the RDS on the Co
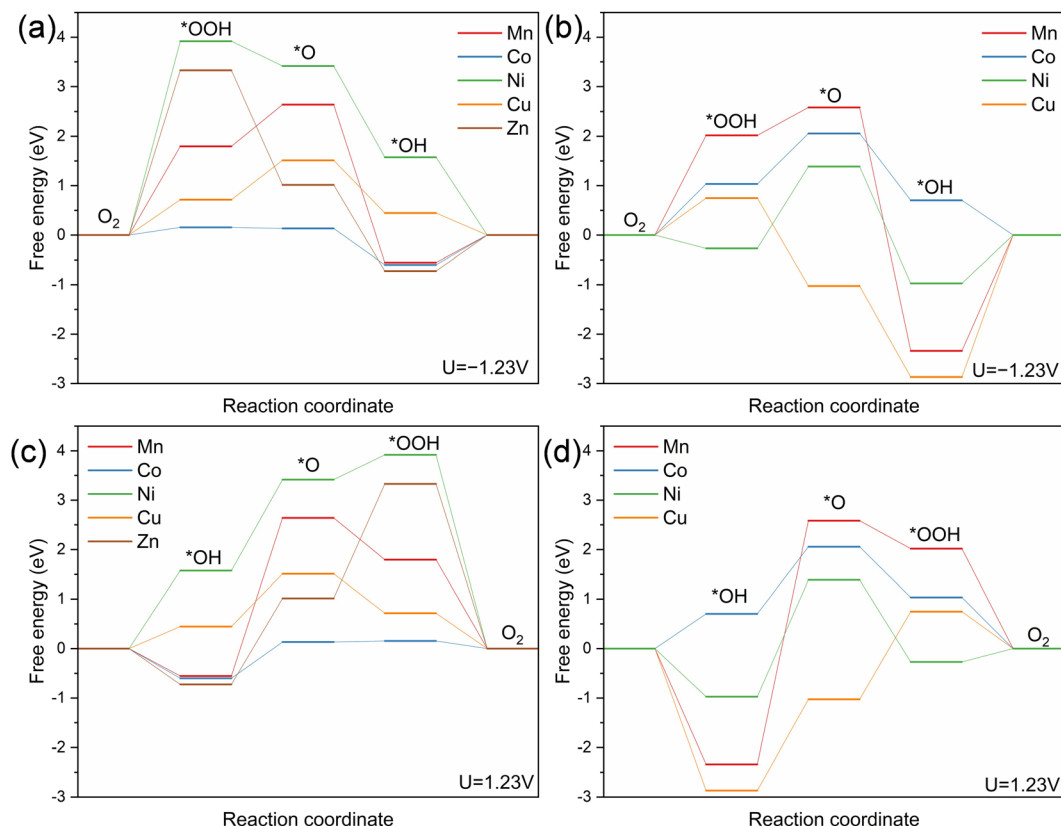
Fig. 7 The adsorption energy distribution diagram of each metal site on $(MnNiCuCoZn)F_2$ and $(MnNiCuCo)F_2$. The (a and b) ORR process and (c and d) OER process.

site of $(MnNiCuCoZn)F_2$ exhibits a ΔG value of 0.73 eV, which is lower than those on Zn ($\Delta G = 2.31$ eV), Cu ($\Delta G = 1.06$ eV), Ni ($\Delta G = 1.84$ eV), and Mn ($\Delta G = 3.19$ eV) sites. Therefore, the Co site can contribute to higher OER catalytic activity when compared to other metal sites in $(MnNiCuCoZn)F_2$. The energy barriers of the RDS for various metal atoms in $(MnNiCuCo)F_2$ are Co ($\Delta G = 1.35$ eV), Cu ($\Delta G = 1.84$ eV), Ni ($\Delta G = 2.36$ eV), and Mn ($\Delta G = 4.92$ eV), respectively. The Co component in both $(MnNiCuCo)F_2$ and $(MnNiCuCoZn)F_2$ exhibits a vital role in the OER process. These results indicate that Zn significantly reduces the activation energy required for the deprotonation of *OH on Co atoms (1.35 eV → 0.73 eV), thereby significantly enhancing the OER kinetics of $(MnNiCuCoZn)F_2$.

4 Conclusion

Uniformly loaded high-entropy fluoride nanoparticles on porous carbon nanofibers ($(MnNiCuCoZn)F_2$-PCNFs) were successfully designed and prepared through electrostatic spinning and calcination processes. Partial loss of the zinc component induced a transformation of high-entropy fluoride nanoparticles from single-crystal into polycrystalline. The prepared $(MnNiCuCoZn)F_2$-PCNFs, with their continuous conductive pathways and porous morphology, provided an ideal site with high catalytic efficiency for electrocatalytic processes. And the multi-principal element nature of high-entropy materials can also offer a variety of active sites to effectively promote

the electrocatalytic processes of the ORR and OER. Meanwhile, the "polycrystalline transformation" further increased the exposure opportunities of active sites. Consequently, the prepared $(MnNiCuCoZn)F_2$-PCNFs exhibited outstanding electrocatalytic activity for the ORR ($E_{1/2} = 0.852$ V $vs.$ RHE) and OER ($\eta_{10} = 310$ mV). Consequently, the assembled ZABs demonstrated a peak power density of 206 mW cm^{-2}, a specific capacity of 760 mA h g^{-1} and a stable charge–discharge cycle life of over 400 h. The role of $(MnNiCuCoZn)F_2$-PCNFs in enhancing electrocatalytic performance was explored through the DFT calculations. The zinc component in $(MnNiCuCoZn)F_2$-PCNFs led to a more continuous distribution of electronic states at the Fermi level, facilitating electron transfer. Additionally, the zinc component optimized the energy layout of reaction intermediates, significantly reducing the energy barriers for the ORR and OER (from 1.80 eV to 1.03 eV for the ORR, and from 1.35 eV to 0.73 eV for the OER), thereby effectively enhancing oxygen electrocatalytic activity.

Data availability

The data supporting this article have been included as part of the ESI.†

Conflicts of interest

There are no conflicts to declare.

19118 | *J. Mater. Chem. A*, 2024, **12**, 19109–19122

This journal is © The Royal Society of Chemistry 2024

Acknowledgements

References

1 Z. P. Cano, D. Banham, S. Ye, A. Hintennach, J. Lu, M. Fowler and Z. Chen, Batteries and fuel cells for emerging electric vehicle markets, *Nat. Energy*, 2018, **3**(4), 279–289, DOI: 10.1038/s41560-018-0108-1.

2 Z. W. Seh, J. Kibsgaard, C. F. Dickens, I. Chorkendorff, J. K. Norskov and T. F. Jaramillo, Combining theory and experiment in electrocatalysis: Insights into materials design, *Science*, 2017, **355**(6321), eaad4998, DOI: 10.1126/science.aad4998.

3 Y.-P. Deng, R. Liang, G. Jiang, Y. Jiang, A. Yu and Z. Chen, The current state of aqueous Zn-based rechargeable batteries, *ACS Energy Lett.*, 2020, **5**(5), 1665–1675, DOI: 10.1021/acsenergylett.0c00502.

4 B. J. Hopkins, C. N. Chervin, J. W. Long, D. R. Rolison and J. F. Parker, Projecting the specific energy of rechargeable zinc–air batteries, *ACS Energy Lett.*, 2020, **5**(11), 3405–3408, DOI: 10.1021/acsenergylett.0c01994.

5 J. Fu, R. Liang, G. Liu, A. Yu, Z. Bai, L. Yang and Z. Chen, Recent progress in electrically rechargeable zinc-air batteries, *Adv. Mater.*, 2019, **31**(31), e1805230, DOI: 10.1002/adma.201805230.

6 C. X. Zhao, J. N. Liu, B. Q. Li, D. Ren, X. Chen, J. Yu and Q. Zhang, Multiscale construction of bifunctional electrocatalysts for long-lifespan rechargeable zinc–air batteries, *Adv. Funct. Mater.*, 2020, **30**(36), 2003619, DOI: 10.1002/adfm.202003619.

7 L. Sun, Q. Wang, M. Ma, H. Xie and X. Zhou, Etching-assisted synthesis of single atom Ni-tailored Pt nanocatalyst enclosed by high-index facets for active and stable oxygen reduction catalysis, *Nano Energy*, 2022, **103**, 107800, DOI: 10.1016/j.nanoen.2022.107800.

8 Y. Wei, H. Huang, F. Gao and G. Jiang, 2D transitional-metal nickel compounds monolayer: Highly efficient multifunctional electrocatalysts for the HER, OER and ORR, *Int. J. Hydrogen Energy*, 2023, **48**(11), 4242–4252, DOI: 10.1016/j.ijhydene.2022.10.250.

9 K. Gong, F. Du, Z. Xia, M. Durstock and L. Dai, Nitrogen-doped carbon nanotube arrays with high electrocatalytic activity for oxygen reduction, *Science*, 2009, **323**, 760–764.

10 D. Deng, L. Yu, X. Chen, G. Wang, L. Jin, X. Pan, J. Deng, G. Sun and X. Bao, Iron encapsulated within pod-like carbon nanotubes for oxygen reduction reaction, *Angew. Chem., Int. Ed.*, 2013, **52**(1), 371–375, DOI: 10.1002/anie.201204958.

11 Z. Qian, Y. Chen, Z. Tang, Z. Liu, X. Wang, Y. Tian and W. Gao, Hollow Nanocages of $Ni_xCo_{1-x}Se$ for Efficient Zinc-Air Batteries and Overall Water Splitting, *Nano-Micro Lett.*, 2019, **11**(1), 28, DOI: 10.1007/s40820-019-0258-0.

12 F. Yang, J. Xie, D. Rao, X. Liu, J. Jiang and X. Lu, Octahedral distortion enhances exceptional oxygen catalytic activity of calcium manganite for advanced Zn-Air batteries, *Nano Energy*, 2021, **85**, 106020, DOI: 10.1016/j.nanoen.2021.106020.

13 X. Zheng, J. Zhang, J. Wang, Z. Zhang, W. Hu and Y. Han, Facile synthesis of nickel cobalt selenide hollow nanospheres as efficient bifunctional electrocatalyst for rechargeable Zn-air battery, *Sci. China Mater.*, 2019, **63**(3), 347–355, DOI: 10.1007/s40843-019-1203-0.

14 Y. Wang, J. Wu, S. Tang, J. Yang, C. Ye, J. Chen, Y. Lei and D. Wang, Synergistic Fe-Se atom pairs as bifunctional oxygen electrocatalysts boost low-temperature rechargeable Zn-air battery, *Angew. Chem., Int. Ed.*, 2023, **62**(15), e202219191, DOI: 10.1002/anie.202219191.

15 X. Wu, Q. Wang, S. Yang, J. Zhang, Y. Cheng, H. Tang, L. Ma, X. Min, C. Tang, S. P. Jiang, F. Wu, Y. Lei, S. Ciampic, S. Wang and L. Dai, Sublayer-enhanced atomic sites of single atom catalysts through *in situ* atomization of metal oxide nanoparticles, *Energy Environ. Sci.*, 2022, **15**(3), 1183–1191, DOI: 10.1039/d1ee03311e.

16 X. Li, X. Yang, H. Xue, H. Pang and Q. Xu, Metal–organic frameworks as a platform for clean energy applications, *EnergyChem*, 2020, **2**(2), 100027, DOI: 10.1016/j.enchem.2020.100027.

17 H.-J. Qiu, G. Fang, J. Gao, Y. Wen, J. Lv, H. Li, G. Xie, X. Liu and S. Sun, Noble metal-free nanoporous high-entropy alloys as highly efficient electrocatalysts for oxygen evolution reaction, *ACS Mater. Lett.*, 2019, **1**(5), 526–533, DOI: 10.1021/acsmaterialslett.9b00414.

18 T. Wang, H. Chen, Z. Yang, J. Liang and S. Dai, High-entropy perovskite fluorides: a new platform for oxygen evolution catalysis, *J. Am. Chem. Soc.*, 2020, **142**(10), 4550–4554, DOI: 10.1021/jacs.9b12377.

19 X. Sun, Y. Zhang, P. Song, J. Pan, L. Zhuang, W. Xu and W. Xing, Fluorine-doped carbon blacks: highly efficient metal-free electrocatalysts for oxygen reduction reaction, *ACS Catal.*, 2013, **3**(8), 1726–1729, DOI: 10.1021/cs400374k.

20 B. Singh, M. B. Gawande, A. D. Kute, R. S. Varma, P. Fornasiero, P. McNeice, R. V. Jagadeesh, M. Beller and R. Zboril, Single-atom (iron-based) catalysts: synthesis and applications, *Chem. Rev.*, 2021, **121**(21), 13620–13697, DOI: 10.1021/acs.chemrev.1c00158.

21 J. Zhang, Q. Xu, J. Wang, Y. Li, H. Jiang and C. Li, Dual-defective Co_3O_4 nanoarrays enrich target intermediates and promise high-efficient overall water splitting, *Chem. Eng. J.*, 2021, **424**, 130328, DOI: 10.1016/j.cej.2021.130328.

22 S. S. Aamlid, M. Oudah, J. Rottler and A. M. Hallas, Understanding the role of entropy in high entropy oxides, *J. Am. Chem. Soc.*, 2023, **145**(11), 5991–6006, DOI: 10.1021/jacs.2c11608.

This journal is © The Royal Society of Chemistry 2024

J. Mater. Chem. A, 2024, **12**, 19109–19122 | **19119**

23 J. Yeh, Alloy design strategies and future trends in high-entropy alloys, *J. Miner. Met. Mater. Soc.*, 2013, **65**(12), 1759–1771, DOI: **10.1007/s11837-013-0761-6**.

24 Y. Yao, Z. Li, P. Xie, Z. Huang, T. Li, D. Morris, Z. Finfrock, J. Zhou, M. Jiao, J. Gao and Y. Ma, Computationally aided, entropy-driven synthesis of highly efficient and durable multi-elemental alloy catalysts, *Sci. Adv.*, 2020, **6**, eaaz0510.

25 J. Yeh, S. Chang, Y. Hong, S. Chen and S. Lin, Anomalous decrease in X-ray diffraction intensities of Cu–Ni–Al–Co–Cr–Fe–Si alloy systems with multi-principal elements, *Mater. Chem. Phys.*, 2007, **103**(1), 41–46, DOI: **10.1016/j.matchemphys.2007.01.003**.

26 K. Y. Tsai, M. H. Tsai and J. W. Yeh, Sluggish diffusion in Co–Cr–Fe–Mn–Ni high-entropy alloys, *Acta Mater.*, 2013, **61**(13), 4887–4897, DOI: **10.1016/j.actamat.2013.04.058**.

27 H. Zheng, G. Luo, A. Zhang, X. Lu and L. He, The synthesis and catalytic applications of nanosized high-entropy alloys, *ChemCatChem*, 2020, **13**(3), 806–817, DOI: **10.1002/cctc.202001163**.

28 Y. Ma, H. Li, H. Wang, X. Mao, V. Linkov, S. Ji, O. U. Gcilitshana and R. Wang, Evolution of the electrocatalytic activity of carbon-supported amorphous platinum–ruthenium–nickel–phosphorous nanoparticles for methanol oxidation, *J. Power Sources*, 2014, **268**, 498–507, DOI: **10.1016/j.jpowsour.2014.06.091**.

29 G. Fang, J. Gao, J. Lv, H. Jia, H. Li, W. Liu, G. Xie, Z. Chen, Y. Huang, Q. Yuan, X. Liu, X. Lin, S. Sun and H.-J. Qiu, Multi-component nanoporous alloy/(oxy)hydroxide for bifunctional oxygen electrocatalysis and rechargeable Zn-air batteries, *Appl. Catal., B*, 2020, **268**, 118431, DOI: **10.1016/j.apcatb.2019.118431**.

30 T. Löffler, H. Meyer, A. Savan, P. Wilde, A. Garzón Manjón, Y. T. Chen, E. Ventosa, C. Scheu, A. Ludwig and W. Schuhmann, Discovery of a multinary noble metal–free oxygen reduction catalyst, *Adv. Energy Mater.*, 2018, **8**(34), 1802269, DOI: **10.1002/aenm.201802269**.

31 L. Sharma, N. K. Katiyar, A. Parui, R. Das, R. Kumar, C. S. Tiwary, A. K. Singh, A. Halder and K. Biswas, Low-cost high entropy alloy (HEA) for high-efficiency oxygen evolution reaction (OER), *Nano Res.*, 2021, **15**(6), 4799–4806, DOI: **10.1007/s12274-021-3802-4**.

32 S. Chen, H. Ren, Y. Qiu, C. Luo, Q. Zhao and W. Yang, Engineering bifunctional electrocatalysts for rechargeable Zn-Air battery by confining Co–Zn–Mn in flower-structured carbon, *J. Power Sources*, 2023, **573**, 233116, DOI: **10.1016/j.jpowsour.2023.233116**.

33 C. Wang, M. Zhu, Z. Cao, P. Zhu, Y. Cao, X. Xu, C. Xu and Z. Yin, Heterogeneous bimetallic sulfides based seawater electrolysis towards stable industrial-level large current density, *Appl. Catal., B*, 2021, **291**, 120071, DOI: **10.1016/j.apcatb.2021.120071**.

34 X. F. Lu, S. L. Zhang, W. L. Sim, S. Gao and X. W. D. Lou, Phosphorized $CoNi_2S_4$ yolk-shell spheres for highly efficient hydrogen production *via* water and urea electrolysis, *Angew. Chem., Int. Ed.*, 2021, **60**(42), 22885–22891, DOI: **10.1002/anie.202108563**.

35 J. Ju, N. Deng, D. Zhang, J. Yan, L. Li, W. Kang and B. Cheng, Facile construction of PCNF&CNT composite material by one-step simultaneous carbonization and chemical vapor deposition, *J. Mater. Sci.*, 2019, **54**(2), 1616–1628, DOI: **10.1007/s10853-018-2932-x**.

36 G. Wang, S. Jia, H. Gao, Y. Shui, J. Fan, Y. Zhao, L. Li, W. Kang, N. Deng and B. Cheng, The action mechanisms and structures designs of F-containing functional materials for high performance oxygen electrocatalysis, *J. Energy Chem.*, 2023, **76**, 377–397, DOI: **10.1016/j.jechem.2022.09.038**.

37 J. Kim, P. C. Shih, Y. Qin, Z. Al-Bardan, C. J. Sun and H. Yang, A porous pyrochlore $Y_2[Ru_{1.6}Y_{0.4}]O_{7-delta}$ electrocatalyst for enhanced performance towards the oxygen evolution reaction in acidic media, *Angew Chem. Int. Ed. Engl.*, 2018, **57**(42), 13877–13881, DOI: **10.1002/anie.201808825**.

38 D. Li, C. Wang, D. S. Strmcnik, D. V. Tripkovic, X. Sun, Y. Kang, M. Chi, J. D. Snyder, D. van der Vliet, Y. Tsai, V. R. Stamenkovic, S. Sun and N. M. Markovic, Functional links between Pt single crystal morphology and nanoparticles with different size and shape: the oxygen reduction reaction case, *Energy Environ. Sci.*, 2014, **7**(12), 4061–4069, DOI: **10.1039/c4ee01564a**.

39 X. Zang, W. Chen, X. Zou, J. N. Hohman, L. Yang, B. Li, M. Wei, C. Zhu, J. Liang, M. Sanghadasa, J. Gu and L. Lin, Self-Assembly of Large-Area 2D Polycrystalline Transition Metal Carbides for Hydrogen Electrocatalysis, *Adv. Mater.*, 2018, **30**(50), e1805188, DOI: **10.1002/adma.201805188**.

40 C. Dette, M. R. Hurst, J. Deng, M. R. Nellist and S. W. Boettcher, Structural Evolution of Metal (Oxy) hydroxide Nanosheets during the Oxygen Evolution Reaction, *ACS Appl. Mater. Interfaces*, 2019, **11**(6), 5590–5594, DOI: **10.1021/acsami.8b02796**.

41 M. Kaftory, M. Botoshansky, M. Kapon and V. Shteiman, Irreversible single-crystal to polycrystal and reversible single-crystal to single-crystal phase transformations in cyanurates, *Acta Crystallogr., Sect. B: Struct. Sci.*, 2001, **57**, 791–799.

42 J. A. Dean and N. A. Lange, *Lange's Handbook of Chemistry*, McGraw-Hill inc., 1998.

43 T. Liu, D. Liu, F. Qu, D. Wang, L. Zhang, R. Ge, S. Hao, Y. Ma, G. Du, A. M. Asiri, L. Chen and X. Sun, Enhanced electrocatalysis for energy-efficient hydrogen production over CoP catalyst with nonelectroactive Zn as a promoter, *Adv. Energy Mater.*, 2017, **7**(15), 1700020, DOI: **10.1002/aenm.201700020**.

44 W. He, H. Liu, J. Cheng, J. Mao, C. Chen, Q. Hao, J. Zhao, C. Liu, Y. Li and L. Liang, Designing Zn-doped nickel sulfide catalysts with an optimized electronic structure for enhanced hydrogen evolution reaction, *Nanoscale*, 2021, **13**(22), 10127–10132, DOI: **10.1039/d1nr01726h**.

45 R. Guo, Y. Yang, C. Zhao, F. Huo, J. Xue, J. He, B. Sun, Z. Sun, H. K. Liu and S. X. Dou, The role of high-entropy materials in lithium-based rechargeable batteries, *Adv. Funct. Mater.*, 2023, 2313168, DOI: **10.1002/adfm.202313168**.

46 K. Dong, J. Liang, Y. Wang, Z. Xu, Q. Liu, Y. Luo, T. Li, L. Li, X. Shi, A. M. Asiri, Q. Li, D. Ma and X. Sun, Honeycomb

19120 | *J. Mater. Chem. A*, 2024, **12**, 19109–19122

This journal is © The Royal Society of Chemistry 2024

carbon nanofibers: a superhydrophilic O_2-entrapping electrocatalyst enables ultrahigh mass activity for the two-electron oxygen reduction reaction, *Angew. Chem., Int. Ed.*, 2021, **60**(19), 10583–10587, DOI: **10.1002/anie.202101880**.

47 G. Wang, H. Chi, Y. Feng, J. Fan, N. Deng, W. Kang and B. Cheng, MnF_2 surface modulated hollow carbon nanorods on porous carbon nanofibers as efficient bi-functional oxygen catalysis for rechargeable zinc–air batteries, *Small*, 2023, e2306367, DOI: **10.1002/smll.202306367**.

48 S. L. Dudarev, G. A. Botton, S. Y. Savrasov, C. J. Humphreys and A. P. Sutton, Electron-energy-loss spectra and the structural stability of nickel oxide: An LSDA+U study, *Phys. Rev. B: Condens. Matter*, 1998, **57**(3), 1505–1509.

49 V. V. Anisimov, J. Zaanen and O. K. Andersen, Band theory and mott insulators: hubbard U instead of stoner I, *Phys. Rev. B: Condens. Matter*, 1991, **44**(3), 943–954, DOI: **10.1103/physrevb.44.943**.

50 M. A. Alkhalifah, B. Howchen, J. Staddon, V. Celorrio, D. Tiwari and D. J. Fermin, Correlating orbital composition and activity of $LaMn_xNi_{1-x}O_3$ nanostructures toward oxygen electrocatalysis, *J. Am. Chem. Soc.*, 2022, **144**(10), 4439–4447, DOI: **10.1021/jacs.1c11757**.

51 S. Kattel, B. Yan, Y. Yang, J. G. Chen and P. Liu, Optimizing binding energies of key intermediates for CO_2 hydrogenation to methanol over oxide-supported copper, *J. Am. Chem. Soc.*, 2016, **138**(38), 12440–12450, DOI: **10.1021/jacs.6b05791**.

52 R. Zhang, L. Pan, B. Guo, Z. F. Huang, Z. Chen, L. Wang, X. Zhang, Z. Guo, W. Xu, K. P. Loh and J. J. Zou, Tracking the role of defect types in Co_3O_4 structural evolution and active motifs during oxygen evolution reaction, *J. Am. Chem. Soc.*, 2023, **145**(4), 2271–2281, DOI: **10.1021/jacs.2c10515**.

53 J. Zhang, H. B. Yang, D. Zhou and B. Liu, Adsorption energy in oxygen electrocatalysis, *Chem. Rev.*, 2022, **122**(23), 17028–17072, DOI: **10.1021/acs.chemrev.1c01003**.

54 W. Wu, S. Luo, Y. Huang, H. He, P. K. Shen and J. Zhu, Recent advances in transition metal phosphide-based heterostructure electrocatalysts for the oxygen evolution reaction, *Mater. Chem. Front.*, 2024, **8**(4), 1064–1083, DOI: **10.1039/d3qm00793f**.

55 S. Kang, K. Lee, J. H. Ryu, G. Ali, M. Akbar, K. Y. Chung, C.-Y. Chung, H. Han and K. M. Kim, Transition Metal Compounds on Functionalized Multiwall Carbon Nanotubes for the Efficient Oxygen Evolution Reaction, *ACS Appl. Nano Mater.*, 2023, **6**(6), 4319–4327, DOI: **10.1021/acsanm.2c05458**.

56 G. Huang, M. Hu, X. Xu, A. A. Alothman, M. S. S. Mushab, S. Ma, P. K. Shen, J. Zhu and Y. Yamauchi, Optimizing Heterointerface of $Co_2P–Co_xO_y$ Nanoparticles within a Porous Carbon Network for Deciphering Superior Water Splitting, *Small Struct.*, 2023, **4**(6), 202200235, DOI: **10.1002/sstr.202200235**.

57 X. Fan, Y. Liu, S. Chen, J. Shi, J. Wang, A. Fan, W. Zan, S. Li, W. A. Goddard and X.-M. Zhang, Defect-enriched iron fluoride-oxide nanoporous thin films bifunctional catalyst for water splitting, *Nat. Commun.*, 2018, **9**(1), 1809, DOI: **10.1038/s41467-018-04248-y**.

58 A. Sarkar, L. Velasco, D. Wang, Q. Wang, G. Talasila, L. de Biasi, C. Kubel, T. Brezesinski, S. S. Bhattacharya, H. Hahn and B. Breitung, High entropy oxides for reversible energy storage, *Nat. Commun.*, 2018, **9**(1), 3400, DOI: **10.1038/s41467-018-05774-5**.

59 B. Fultz, Vibrational thermodynamics of materials, *Prog. Mater. Sci.*, 2010, **55**(4), 247–352, DOI: **10.1016/j.pmatsci.2009.05.002**.

60 R. Gan, Y. Song, C. Ma and J. Shi, In situ growth of N-doped carbon nanotubes in $Fe-N_x/Fe_2O_3/Fe_3O_4$-encapsulated carbon sheets for efficient bifunctional oxygen catalysis, *Appl. Catal., B*, 2023, **327**, 122443, DOI: **10.1016/j.apcatb.2023.122443**.

61 L. Tang, X. Meng, D. Deng and X. Bao, Confinement catalysis with 2D materials for energy conversion, *Adv. Mater.*, 2019, **31**(50), e1901996, DOI: **10.1002/adma.201901996**.

62 T. Zhou, H. Shan, H. Yu, C. a. Zhong, J. Ge, N. Zhang, W. Chu, W. Yan, Q. Xu, H. a. Wu, C. Wu and Y. Xie, Nanopore confinement of electrocatalysts optimizing triple transport for an ultrahigh-power-density zinc-air fuel cell with robust stability, *Adv. Mater.*, 2020, **32**(47), 2003251, DOI: **10.1002/adma.202003251**.

63 Y.-H. Lee, F. Li, K.-H. Chang, C.-C. Hu and T. Ohsaka, Novel synthesis of N-doped porous carbons from collagen for electrocatalytic production of H_2O_2, *Appl. Catal., B*, 2012, **126**, 208–214, DOI: **10.1016/j.apcatb.2012.06.031**.

64 J. A. Prithi, N. Rajalakshmi and G. Ranga Rao, Nitrogen doped mesoporous carbon supported Pt electrocatalyst for oxygen reduction reaction in proton exchange membrane fuel cells, *Int. J. Hydrogen Energy*, 2018, **43**(9), 4716–4725, DOI: **10.1016/j.ijhydene.2017.11.137**.

65 S. Dilpazir, R. Liu, M. Yuan, M. Imran, Z. Liu, Y. Xie, H. Zhao and G. Zhang, Br/Co/N Co-doped porous carbon frameworks with enriched defects for high-performance electrocatalysis, *J. Mater. Chem. A*, 2020, **8**(21), 10865–10874, DOI: **10.1039/d0ta02411b**.

66 T. Xiong, J. Li, J. Chandra Roy, M. Koroma, Z. Zhu, H. Yang, L. Zhang, T. Ouyang, M. S. Balogun and M. Al-Mamun, Hetero-interfacial nickel nitride/vanadium oxynitride porous nanosheets as trifunctional electrodes for HER, OER and sodium ion batteries, *J. Energy Chem.*, 2023, **81**, 71–81, DOI: **10.1016/j.jechem.2023.01.064**.

67 F. Ma, Q. Wu, M. Liu, L. Zheng, F. Tong, Z. Wang, P. Wang, Y. Liu, H. Cheng, Y. Dai, Z. Zheng, Y. Fan and B. Huang, Surface fluorination engineering of NiFe prussian blue analogue derivatives for highly efficient oxygen evolution reaction, *ACS Appl. Mater. Interfaces*, 2021, **13**(4), 5142–5152, DOI: **10.1021/acsami.0c20886**.

68 Y. Feng, B. Zhong, R. Zhang, J. Yu, Z. Huang, Y. Huang, Z. Wu, Y. Fan, J. Tian, W. Xie and K. Zhang, Taming active-ion crosstalk by targeted ion sifter toward high-voltage lithium metal batteries, *Adv. Energy Mater.*, 2023, **13**(45), 2302295, DOI: **10.1002/aenm.202302295**.

This journal is © The Royal Society of Chemistry 2024

J. Mater. Chem. A, 2024, **12**, 19109–19122 | **19121**

69 W. Ma, S. Xie, T. Liu, Q. Fan, J. Ye, F. Sun, Z. Jiang, Q. Zhang, J. Cheng and Y. Wang, Electrocatalytic reduction of CO_2 to ethylene and ethanol through hydrogen-assisted C–C coupling over fluorine-modified copper, *Nat. Catal.*, 2020, **3**(6), 478–487, DOI: **10.1038/s41929-020-0450-0**.

70 J. Zhang and L. Dai, Nitrogen, phosphorus, and fluorine tri-doped graphene as a multifunctional catalyst for self-powered electrochemical water splitting, *Angew. Chem., Int. Ed.*, 2016, **55**(42), 13296–13300, DOI: **10.1002/anie.201607405**.

71 Y. Chang, J. Chen, J. Jia, X. Hu, H. Yang, M. Jia and Z. Wen, The fluorine-doped and defects engineered carbon nanosheets as advanced electrocatalysts for oxygen electroreduction, *Appl. Catal., B*, 2021, **284**, 119721, DOI: **10.1016/j.apcatb.2020.119721**.

72 J. Li, M. Chen, D. A. Cullen, S. Hwang, M. Wang, B. Li, K. Liu, S. Karakalos, M. Lucero, H. Zhang, C. Lei, H. Xu, G. E. Sterbinsky, Z. Feng, D. Su, K. L. More, G. Wang, Z. Wang and G. Wu, Atomically dispersed manganese catalysts for oxygen reduction in proton-exchange membrane fuel cells, *Nat. Catal.*, 2018, **1**(12), 935–945, DOI: **10.1038/s41929-018-0164-8**.

73 Y. Leng, B. Yang, Y. Zhao and Z. Xiang, Fluorinated bimetallic nanoparticles decorated carbon nanofibers as highly active and durable oxygen electrocatalyst for fuel cells, *J. Energy Chem.*, 2022, **73**, 549–555, DOI: **10.1016/j.jechem.2022.04.026**.

74 S. G. Peera, A. Arunchander and A. K. Sahu, Platinum nanoparticles supported on nitrogen and fluorine co-doped graphite nanofibers as an excellent and durable oxygen reduction catalyst for polymer electrolyte fuel cells, *Carbon*, 2016, **107**, 667–679, DOI: **10.1016/j.carbon.2016.06.021**.

75 F. T. Haase, A. Rabe, F. P. Schmidt, A. Herzog, H. S. Jeon, W. Frandsen, P. V. Narangoda, I. Spanos, K. Friedel Ortega, J. Timoshenko, T. Lunkenbein, M. Behrens, A. Bergmann, R. Schlögl and B. Roldan Cuenya, Role of nanoscale inhomogeneities in Co_2FeO_4 catalysts during the oxygen evolution reaction, *J. Am. Chem. Soc.*, 2022, **144**(27), 12007–12019, DOI: **10.1021/jacs.2c00850**.

76 Y. Fang and Z. Liu, Mechanism and tafel lines of electro-oxidation of water to oxygen on $RuO_2(110)$, *J. Am. Chem. Soc.*, 2010, **132**, 18214–18222.

77 X. Huang, Y. Zhang, H. Shen, W. Li, T. Shen, Z. Ali, T. Tang, S. Guo, Q. Sun and Y. Hou, N-Doped Carbon Nanosheet Networks with Favorable Active Sites Triggered by Metal Nanoparticles as Bifunctional Oxygen Electrocatalysts, *ACS Energy Lett.*, 2018, **3**(12), 2914–2920, DOI: **10.1021/acsenergylett.8b01717**.

78 R. He, L. Yang, Y. Zhang, D. Jiang, S. Lee, S. Horta, Z. Liang, X. Lu, A. Ostovari Moghaddam, J. Li, M. Ibanez, Y. Xu, Y. Zhou and A. Cabot, A 3d-4d-5d High Entropy Alloy as a Bifunctional Oxygen Catalyst for Robust Aqueous Zinc-Air Batteries, *Adv. Mater.*, 2023, e2303719, DOI: **10.1002/adma.202303719**.

79 H. Gong, X. Zheng, K. Zeng, B. Yang, X. Liang, L. Li, Y. Tao and R. Yang, Ni_3Fe nanoalloys embedded in N-doped carbon derived from dual-metal ZIF: Efficient bifunctional electrocatalyst for Zn–air battery, *Carbon*, 2021, **174**, 475–483, DOI: **10.1016/j.carbon.2020.12.053**.

80 Z. Zhu, L. Luo, Y. He, M. Mushtaq, J. Li, H. Yang, Z. Khanam, J. Qu, Z. Wang and M. S. Balogun, High-Performance Alkaline Freshwater and Seawater Hydrogen Catalysis by Sword-Head Structured Mo_2N-Ni_3Mo_3N Tunable Interstitial Compound Electrocatalysts, *Adv. Funct. Mater.*, 2023, **34**, 202306061, DOI: **10.1002/adfm.202306061**.

81 T. Xiong, Z. Zhu, Y. He, M. S. Balogun and Y. Huang, Phase Evolution on the Hydrogen Adsorption Kinetics of NiFe-Based Heterogeneous Catalysts for Efficient Water Electrolysis, *Small Methods*, 2023, e2201472, DOI: **10.1002/smtd.202201472**.

82 Y. Meng, W. Song, H. Huang, Z. Ren, S. Y. Chen and S. L. Suib, Structure-property relationship of bifunctional MnO_2 nanostructures: highly efficient, ultra-stable electrochemical water oxidation and oxygen reduction reaction catalysts identified in alkaline media, *J. Am. Chem. Soc.*, 2014, **136**(32), 11452–11464, DOI: **10.1021/ja505186m**.

83 C. Ye, J. Liu, Q. Zhang, X. Jin, Y. Zhao, Z. Pan, G. Chen, Y. Qiu, D. Ye, L. Gu, G. I. N. Waterhouse, L. Guo and S. Yang, Activating metal oxides nanocatalysts for electrocatalytic water oxidation by quenching-induced near-surface metal atom functionality, *J. Am. Chem. Soc.*, 2021, **143**(35), 14169–14177, DOI: **10.1021/jacs.1c04737**.

84 Y. Huang, X. Li, P. K. Shen, C. Yang and J. Zhu, High-Performance MoP-Mo_2C/C Heterogeneous Nanoparticle Catalysts for Alkaline Hydrogen Evolution and Oxidation Reactions, *ACS Mater. Lett.*, 2024, **6**(5), 1678–1685, DOI: **10.1021/acsmaterialslett.3c01494**.

85 Y. Zheng, Y. Jiao, A. Vasileff and S. Z. Qiao, The hydrogen evolution reaction in alkaline solution: from theory, single crystal models, to practical electrocatalysts, *Angew. Chem., Int. Ed.*, 2018, **57**(26), 7568–7579, DOI: **10.1002/anie.201710556**.

86 H. Zhang, Y. Liu, T. Chen, J. Zhang, J. Zhang and X. W. D. Lou, Unveiling the activity origin of electrocatalytic oxygen evolution over isolated Ni atoms supported on a N-doped carbon matrix, *Adv. Mater.*, 2019, **31**(48), e1904548, DOI: **10.1002/adma.201904548**.

87 H. Zhu, S. Sun, J. Hao, Z. Zhuang, S. Zhang, T. Wang, Q. Kang, S. Lu, X. Wang, F. Lai, T. Liu, G. Gao, M. Du and D. Wang, A high-entropy atomic environment converts inactive to active sites for electrocatalysis, *Energy Environ. Sci.*, 2023, **16**(2), 619–628, DOI: **10.1039/d2ee03185j**.

88 J. Li, Z. Zhu, Y. Huang, F. Wang and M.-S. Balogun, Ni_3N: A multifunctional material for energy storage and electrocatalysis, *Mater. Today Energy*, 2022, **26**, 101001, DOI: **10.1016/j.mtener.2022.101001**.

89 M. Ha, D. Y. Kim, M. Umer, V. Gladkikh, C. W. Myung and K. S. Kim, Tuning metal single atoms embedded in N_xC_y moieties toward high-performance electrocatalysis, *Energy Environ. Sci.*, 2021, **14**(6), 3455–3468, DOI: **10.1039/d1ee00154j**.

19122 | *J. Mater. Chem. A*, 2024, **12**, 19109–19122

This journal is © The Royal Society of Chemistry 2024